International Journal of Non-Linear Mechanics 75 (2015) 59–66

Contents lists available at ScienceDirect

International Journal of Non-Linear Mechanics

journal homepage: www.elsevier.com/locate/nlm

Coiling of an elastic beam inside a disk: A model for spider-capture silk

Hervé Elettro [a,b], Fritz Vollrath [c], Arnaud Antkowiak [a,b], Sébastien Neukirch [a,b,*]

[a] Centre National de la Recherche Scientifique, UMR 7190, Institut Jean Le Rond d'Alembert, F-75005 Paris, France
[b] Sorbonne Universités, UPMC Univ Paris 06, UMR 7190, Institut Jean Le Rond d'Alembert, F-75005 Paris, France
[c] Oxford Silk Group, Zoology Department, University of Oxford, UK

ARTICLE INFO

Article history:
Received 3 February 2015
Received in revised form
20 March 2015
Accepted 22 March 2015
Available online 30 March 2015

Keywords:
Coiling
Post-buckling
Elastica
Equilibria paths
Continuation
Stability

ABSTRACT

Motivated by recent experimental observations of capillary-induced spooling of fibers inside droplets both in spider capture silk and in synthetic systems, we investigate the behavior of a fiber packed in a drop. Using a simplified 2D model, we provide analytical predictions for the buckling threshold and the deep post-buckling asymptotic behavior. The threshold for spooling is found to be in particularly good agreement with experimental results. We further solve the Elastica equations for a fiber confined in a soft potential, and track the equilibrium paths using numerical continuation techniques. A wealth of different paths corresponding to different symmetries is uncovered, and their stability is finally discussed.

© 2015 Elsevier Ltd. All rights reserved.

1. Introduction

The mechanical properties of spider silk are often presented as outstanding [1,2]. An indeed, most silk threads outperform the best man-made fibers, such a Kevlar, at least in terms of toughness [3]. To a large extent, these properties rely on the molecular architecture of the silk. For example, it has been shown that the building blocks of flagelliform silk involve molecular nanosprings [4]. In 1989 however, a team comprising a zoologist and a physicist reported on coiling and packing of the core filament inside a glue droplet [5]. This *windlass mechanism*, as it was called, provided indirect evidence that the glue droplets may as well play a role in the mechanical response of the silk thread. These results have been a subject of debate in the community, and it is only very recently that the mechanism has been observed to be active in a real spider web, see Fig. 1 (left) [6]. A natural question that arises in this context is the role played by the molecular structure of the silk and the glue in the observed coiling. An experimental answer to this question is provided in Fig. 1 (right), where a micron-sized artificial thread bearing a silicon oil droplet also exhibits the coiling mechanism and packing behavior, therefore demonstrating that capillarity and elasticity are sufficient ingredients to explain the mechanism.

Interestingly, the shape adopted by the filament inside the drop can be as different as a perfectly ordered closely packed annular bundle or a completely disordered tangle. This behavior is reminiscent of the organization of packed wires in rigid [7] and elastic [8] spherical shells, patterns of folded structures such as plant leaves or crumpled paper [9,10], and DNA packing inside capsids [11–13]. The purpose of the present paper is to explore theoretically in a simplified setting the shape and stability of strongly post-buckled states in order to lay down the basis for a deeper understanding of the windlass mechanism.

The paper is organized as follows. In Section 2 we present the problem and the equilibrium equations. In Section 3 we perform a linear stability analysis of the straight beam and predict the buckling threshold. Experimental results are confronted to theoretical in Section 4. Finally, we describe the non-linear response of the system in terms of equilibrium solutions and their stability in Section 5.

2. Model

We consider an elastic beam in interaction with a liquid disk and under the action of a tensile end-load. As indicated in Fig. 2, we restrict to planar deformations of the beam, X and Y denoting the horizontal and vertical directions respectively. The beam has length L and a circular cross-section of radius h. We work under the slender ($L \gg h$) Euler–Bernoulli hypotheses where the beam is considered inextensible and unshearable. Configurations are thus fully described by the position and orientation of the centerline. We use the arc-length $S \in [0, L]$ and note $\theta(S)$ the angle between the tangent of the beam and the horizontal. The presence of the liquid disk generates capillary forces due to the contrast of surface energy, the interaction

* Corresponding author.
E-mail address: sebastien.neukirch@upmc.fr (S. Neukirch).

http://dx.doi.org/10.1016/j.ijnonlinmec.2015.03.008
0020-7462/© 2015 Elsevier Ltd. All rights reserved.

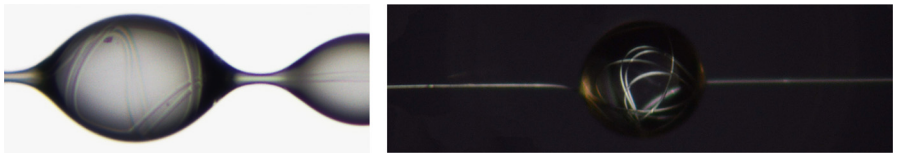

Fig. 1. Experiments on fibers bent inside liquid drops. *Left*: microscopic photograph of spider capture silk. Flagelliform core filaments are seen to be coiled and packed inside a (typically 300μ wide) glue droplet. *Right*: same mechanism reproduced artificially with a 200 μm synthetic droplet and fiber (see experimental verification section in Section 4). Reproduced from [6].

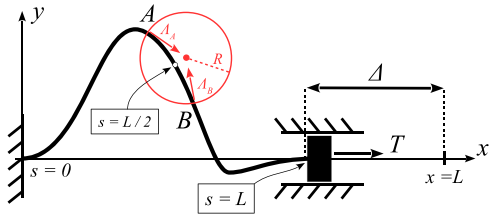

Fig. 2. An elastic beam held in tension at its extremities, and buckling under the action of compressive forces at a disk. The beam is clamped at both ends. The deformation of the beam is described by the angle $\theta(S)$ between the tangent to the beam and the x-axis, where $S \in [0, L]$ is the arc-length along the beam.

energy of the beam with the liquid being smaller than the interaction energy of the beam with the air. Capillary forces are two-fold: (i) meniscus forces applied on the beam at the entrance and exit of the disk, and (ii) barrier forces that prevent the beam from exiting the disk elsewhere than at the meniscus points. We consider that the drop is undeformable and thus remains a disk throughout the experiments. As shown in Appendix A, meniscus forces are pointing toward the center of the disk (see Eqs. (A.15) and (A.18)) and their intensity is related to the angle between their direction and the tangent to the beam at the meniscus points (see Eq. (A.25)). A soft-wall barrier potential [14]

$$V(X,Y) = \frac{V_0}{1+\rho-(1/R)\sqrt{(X-X_C)^2+(Y-Y_C)^2}} \tag{1}$$

is used to retain the beam inside the disk, centered on (X_C, Y_C) and of radius R. The small dimensionless parameter ρ is introduced to avoid the potential to diverge at the meniscus points A and B, where the rod enters and exits the disk. The intensity V_0 of the potential is chosen to be small, the hard-wall limit being $V_0 \to 0$. Kinematics, relating the position (X,Y) of the rod and the inclination $\theta$of its tangent $(\cos\theta, \sin\theta)$ with the horizontal, the bending constitutive relation, relating the curvature $\theta'(S)$ to the moment $M(S)$, and finally force (N_x, N_y) and moment balance are detailed in Appendix A and read

$$X'(S) = \cos\theta, \quad Y'(S) = \sin\theta \tag{2a}$$

$$EI\theta'(S) = M, \quad M'(S) = N_x \sin\theta - N_y \cos\theta \tag{2b}$$

$$N_x'(S) = \chi\frac{\partial V}{\partial X} + \delta(S-S_A)\Lambda_A\frac{X_A-X_C}{R} + \delta(S-S_B)\Lambda_B\frac{X_B-X_C}{R} \tag{2c}$$

$$N_y'(S) = \chi\frac{\partial V}{\partial Y} + \delta(S-S_A)\Lambda_A\frac{Y_A-Y_C}{R} + \delta(S-S_B)\Lambda_B\frac{Y_B-Y_C}{R} \tag{2d}$$

where S is the arc-length along the rod, and $(\,)' = \mathrm{d}(\,)/\mathrm{d}S$. We define the coordinates of point A as $(X_A, Y_A) = (X(S_A), Y(S_A))$, same for point B. Note that the potential V has the dimension of an energy per unit of arc-length of the beam. For $S \in [S_A; S_B]$ the rod lies inside the disk and we have $\chi = 1$, otherwise $\chi = 0$. The Dirac distribution $\delta(S)$ localizes meniscus forces at points A and B. The rod material has Young's modulus E and the second moment of area $I = \pi h^4/4$. The intensities Λ_A and Λ_B of the meniscus forces are unknown but related to surface tension γ_{LV} through Eq. (A.25), where $F_\gamma = 2\pi h\gamma_{LV}\cos\alpha_Y$ with α_Y being the Young–Dupré wetting angle ($\gamma_{SV} - \gamma_{SL} = \gamma_{LV}\cos\alpha_Y$), and where $V_A = V_B = V_0/\rho$ are small compared to F_γ. We restrict ourself to cases where the disk is centered on the mid-point of the rod, that is we introduce Σ such that $S_A = L/2 - \Sigma$ and $S_B = L/2 + \Sigma$. The rod has then 2Σ of its arc-length spent inside the disk. Finally the external applied tension is noted $T = N_x(L)$.

2.1. Non-dimensionalization

We use the diameter $D = 2R$ of the disk as unit length, and the buckling load EI/D^2 as unit force. We thus introduce the following dimensionless quantities:

$$s = \frac{S}{D}; \quad \sigma = \frac{\Sigma}{D}; \quad \ell = \frac{L}{D}; \quad (x,y) = \frac{(X,Y)}{D}; \quad n = \frac{ND^2}{EI}; \quad t = \frac{TD^2}{EI} \tag{3a}$$

$$f_\gamma = \frac{F_\gamma D^2}{EI}; \quad m = \frac{MD}{EI}; \quad \lambda_{A,B} = \frac{\Lambda_{A,B}D^2}{EI}; \quad (v, v_0) = \frac{(V, V_0)D^2}{EI} \tag{3b}$$

and $\delta(s) = D\delta(S)$. We then have

$$v(x,y) = v_0\left(1+\rho-2\sqrt{(x-x_C)^2+(y-y_C)^2}\right)^{-1} \text{ and}$$

$$x'(s) = \cos\theta, \quad y'(s) = \sin\theta \tag{4a}$$

$$\theta'(s) = m, \quad m'(s) = n_x\sin\theta - n_y\cos\theta \tag{4b}$$

$$n_x'(s) = \chi\frac{\partial v}{\partial x} + 2\delta(s-s_A)\lambda_A(x_A-x_C) + 2\delta(s-s_B)\lambda_B(x_B-x_C) \tag{4c}$$

$$n_y'(s) = \chi\frac{\partial v}{\partial y} + 2\delta(s-s_A)\lambda_A(y_A-y_C) + 2\delta(s-s_B)\lambda_B(y_B-y_C) \tag{4d}$$

where $(\,)' = \mathrm{d}(\,)/\mathrm{d}s$, and $s_A = \ell/2 - \sigma$, $s_B = \ell/2 + \sigma$.

2.2. Boundary-value problem

We consider v_0, ρ, f_γ, and ℓ as fixed parameters and we look for equilibrium solutions by integrating (4) with the initial conditions

$$x(0) = 0; \quad y(0) = 0; \quad \theta(0) = 0; \quad m(0) = m_0; \quad n_x(0) = n_{x0};$$

$$n_y(0) = n_{y0} \tag{5}$$

where m_0, n_{x0}, and n_{y0} are unknowns to be accompanied with σ, x_C, y_C, λ_A, and λ_B. We therefore have eight unknowns which are balanced by the following seven conditions. At the $s = \ell$ end of the rod, clamped boundary conditions read

$$y(\ell) = 0; \quad \theta(\ell) = 0 \tag{6}$$

The requirement that points A and B lie on the circle yields the conditions

$$[x_A - x_C]^2 + [y_A - y_C]^2 = 1/4; \quad [x_B - x_C]^2 + [y_B - y_C]^2 = 1/4 \tag{7}$$

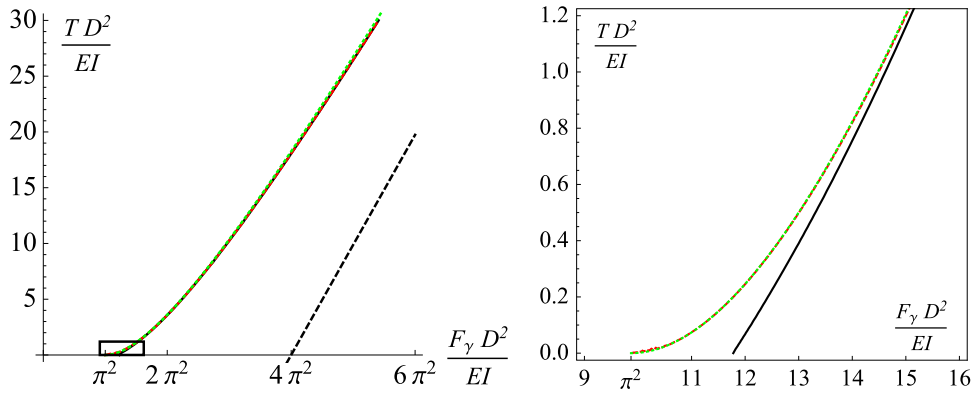

Fig. 3. Buckling curve for $\ell = 5$. (Left) Curves defined by Eqs. (11)–(13). At this scale the three curves are almost indistinguishable. The asymptote $t = f_\gamma - 4\pi^2$ is shown dashed. (Right) Zoom corresponding to the rectangle shown on the Left. The approximations (12) and (13) are still hard to distinguish, but are seen to deviate from the exact curve (11), shown continuous and black.

and the three force balances related to forces coming from the disk read

$$n_x(s_A^-) = n_x(s_B^+) \tag{8a}$$

$$n_y(s_A^-) = n_y(s_B^+) \tag{8b}$$

$$-2f_\gamma + v_A + v_B - 2\lambda_A[(x_A - x_C)\cos\theta(s_A) + (y_A - y_C)\sin\theta(s_A)] + 2\lambda_B[(x_B - x_C)\cos\theta(s_B) + (y_B - y_C)\sin\theta(s_B)] = 0 \tag{8c}$$

The solution set is thus a $8-7=1$ dimensional manifold and we plot in Section 5 different solution paths for several values of the parameter f_γ.

3. Buckling threshold

The trivial solution $x(s) = s$, $y(s) = \theta(s) = m(s) = n_y(s) = 0$ to Eq. (4) with boundary conditions (5)–(8), exists for any value of the load t. Nevertheless, for given values of the parameters v_0, ρ, f_γ, and ℓ, there is a threshold value of t under which the trivial solution ceases to be stable and buckling occurs. We look for the first buckling mode which is symmetrical with respect to the axis joining the center of the disk (x_C, y_C) and the beam midpoint $(x(\ell/2), y(\ell/2))$. We linearize Eqs. (4) for small deflections, $|y(s)| \sim \epsilon$, and small slopes, $|\theta(s)| \sim \epsilon$, with $0 < \epsilon \ll 1$, see Appendix B for a comprehensive exposition of this perturbation expansion. As in the buckling configuration the rod has virtually no packing interaction with the disk, we set $v_0 = 0$. The first four equations of system (4) become $x'(s) = 1$, $y'(s) = \theta(s)$, $\theta'(s) = m(s)$, and $m'(s) = n_x(s)\theta(s) - n_y(s)$. We then have $x_C = \ell/2$, $x_A = \ell/2 - \sigma$, and $x_B = \ell/2 + \sigma$. At order ϵ^0, Eq. (7) yields $\sigma = 1/2$. As symmetry imposes $y_A = y_B$ and $\theta(s_A) = -\theta(s_B)$, Eq. (7) at order ϵ^2 imposes $y_C = y_A = y_B$. Then (8c) at order ϵ^0 yields $2f_\gamma = \lambda_A + \lambda_B$ and, as symmetry requires $\lambda_A = \lambda_B$, we finally obtain $f_\gamma = \lambda_A = \lambda_B$. Following symmetry we introduce $\hat{s} = s - \ell/2$. The three functions $y(\hat{s})$, $\theta(\hat{s})$, and $m(\hat{s})$ are then respectively even, odd, and even functions of the variable $\hat{s}$. We focus on the right half of the system, $\hat{s} \in [0; \ell/2]$. Eq. (4c) is integrated to yield $n_x(\hat{s}) = t - f_\gamma$ for $\hat{s} \in [0; 1/2]$ and $n_x(\hat{s}) = t$ for $\hat{s} \in [1/2; \ell/2]$. Eq. (4d) shows that $n_y(\hat{s}) = \text{const.}$ and from $m'(\hat{s}) = n_x(\hat{s})\theta(\hat{s}) - n_y(\hat{s})$ we see that $n_y(\hat{s})$ has to be odd, hence zero. We finally arrive at the reduced system

$$\theta'' = -(f_\gamma - t)\theta \quad \text{for } \hat{s} \in [0; 1/2] \tag{9}$$

$$\theta'' = t\theta \quad \text{for } \hat{s} \in [1/2; \ell/2] \tag{10}$$

and we restrict to the $f_\gamma > t \geq 0$ case. Integrating these equations and using the boundary conditions $\theta(\hat{s} = 0) = 0 = \theta(\hat{s} = \ell/2)$ and the matching conditions $\theta(\hat{s} = 1/2^-) = \theta(\hat{s} = 1/2^+)$ and $m(\hat{s} = 1/2^-) = m(\hat{s} = 1/2^+)$, we obtain the buckling condition

$$\sqrt{f_\gamma - t}\tanh\frac{(\ell-1)\sqrt{t}}{2} + \sqrt{t}\tan\frac{\sqrt{f_\gamma - t}}{2} = 0 \tag{11}$$

which is plotted in Fig. 3. The two interesting asymptotic limits of the curve defined by (11) are (i) if $t \to 0$ then $f_\gamma \to \pi^2 + 8/\ell$, and (ii) if $f_\gamma \to +\infty$ then $t \to f_\gamma - 4\pi^2$.

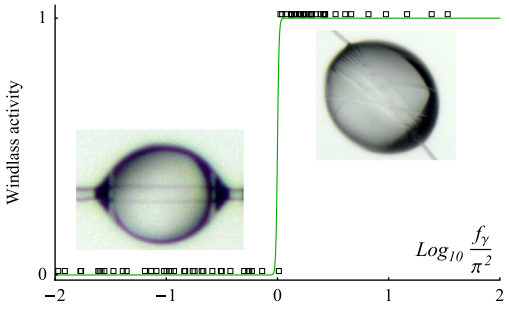

Fig. 4. Experimental verification of the windlass activation as function of the parameter f_γ. The windlass mechanism is active as soon as the meniscus force f_γ is greater than π^2.

3.1. Approximations to the buckling load

In the case where $\ell \gg 1$, we simplify Eq. (11) and find

$$\sqrt{f_\gamma - t} + \sqrt{t}\tan\frac{\sqrt{f_\gamma - t}}{2} = 0 \tag{12}$$

This formula has the same large f_γ limit as (11) and in fact as $\ell \to +\infty$, the curve defined by (11) tends to the curve defined by (12) everywhere but in a boundary layer around $(f_\gamma, t) = (\pi^2, 0)$. Indeed even if ℓ is large, for small t the tanh term cannot be approximated by 1 if $t \sim 1/\ell^2$. It is convenient to have an explicit formula $t = t(f_\gamma)$ for buckling and we introduce the approximation

$$t_b(f_\gamma) = f_\gamma - 4\pi^2 - \frac{108\pi^4}{3\pi^4 - 40\pi^2 + (3\pi^2 - 28)f_\gamma + (32\pi - 6\pi^3)\sqrt{f_\gamma}} \tag{13}$$

This last formula has the same behavior as (12) at low t: we have $t_b(f_\gamma = \pi^2) = 0$, and $t_b'(f_\gamma = \pi^2) = 0$. Moreover (13) also shares the large f_γ limit of (11) and (12): $t_b = -4\pi^2 + f_\gamma + \cdots$. We see in Fig. 3 that the curves defined by (12) and (13) are in fact hard to distinguish.

4. Experimental verification

In order to verify experimentally and quantitatively the mechanics of the windlass, we place a drop on a fiber and test whether the fibre coils in the drop. The fibre is made of BASF Thermoplastic PolyUrethan (TPU) that is melt-spinned. This process involves melting down the TPU, then applying a large extension rate to the liquid filament while it cools down rapidly in the ambient air. It results in reproducible, meter-long micronic fibres (1–20 μm in radius) with portions away from the edges having small perturbations in radius (typically $<5\%$ every 1000 radii). Calipers are used to further manipulate the samples. Clamping is achieved with cured Loctite® glue. The system size is measured optically with a Leica macroscope (VZ85RC) mounted on a micro-step motor and a 3 megapixels Leica DFC-295 camera ($400\times$ magnification, 334 nm/pixel picture resolution) with a Phlox 50×50 mm backlight, at 60,000 lux or alternatively an optical fibre with LED lamp (Moritex MHF-M1002) with circular polarizer. The fibre radius is then extracted by image analysis, using imageJ (http://imagej.nih.gov/ij/). For the droplet, we select silicone oil Rhodorsil 47V1000, the figure 1000 referring to its viscosity compared to water. High viscosity was chosen in order to be able to deposit drops on the fibre by brushing, and for its slow evaporation properties. Using the condition that meniscus forces have to support the weight of the droplet and be strong enough to buckle the beam, we find that to be bendable, a TPU fibre must be below 7.2 μm in radius, with $E_{\mathrm{TPU}}=17\pm3$ MPa, $\gamma_{\mathrm{silicone-oil/air}}=21.1$ mN/m, $\alpha_{Y,\mathrm{silicone-oil/TPU}}=27\pm5^{\circ}$ and $\rho_{\mathrm{silicone-oil}}=960$ kg/m^3 the silicone oil density.

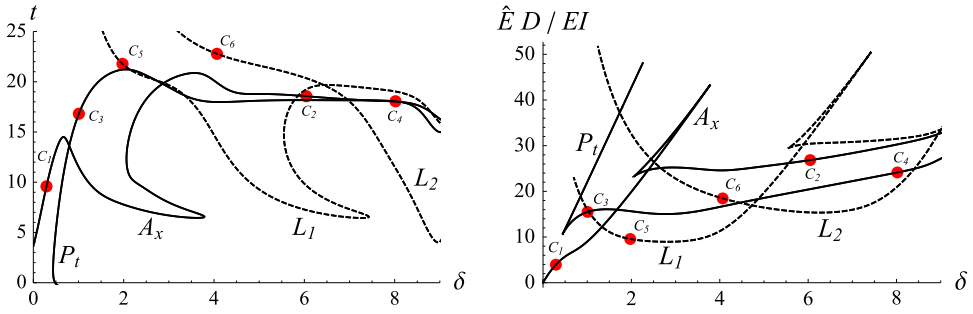

Fig. 5. Post-buckling paths: (*left*) force–displacement curves for $f_\gamma=20$, where t is the applied tension and $\delta$the end-shortening, and (*right*) energy $\hat{E}$ as function of δ. Solid lines represents both *Ax* configurations, where the beam shape is symmetric with respect to the axis joining the center of the disk (x_C,y_C) and the beam midpoint $(x(\ell/2),y(\ell/2))$, and *Pt* configurations, where the beam shape is symmetric with respect to the beam midpoint *Pt*. Dashed lines correspond to L_1 and L_2 configurations.

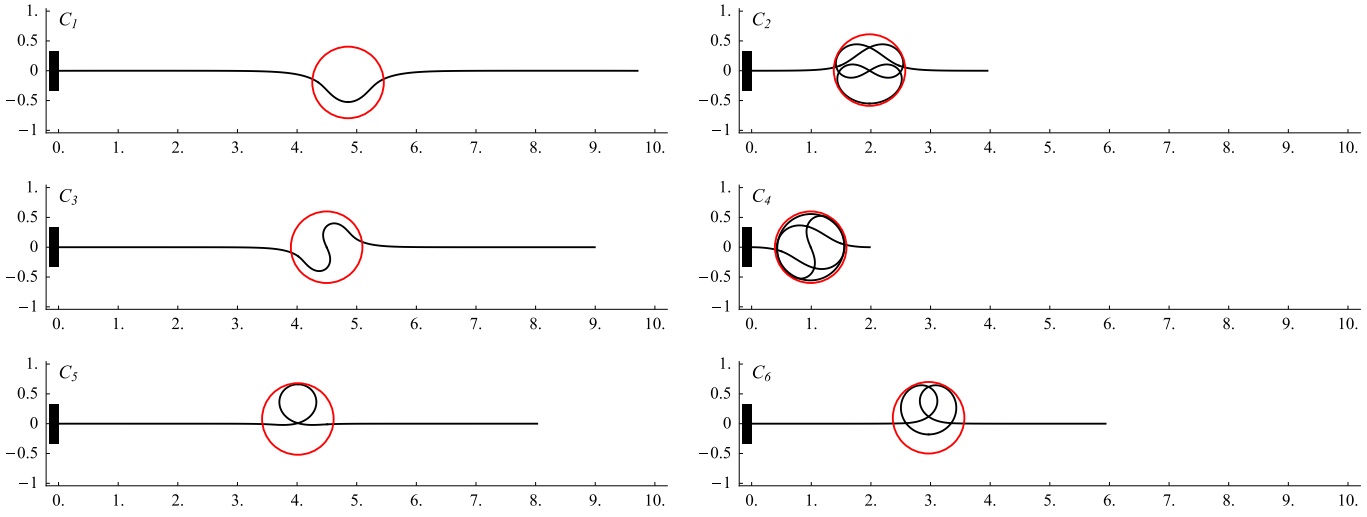

Fig. 6. Post-buckling configurations. Top row shows *Ax* configurations, symmetric with respect to the axis joining the center of the disk (x_C,y_C) and the beam midpoint $(x(\ell/2),y(\ell/2))$. Middle row shows *Pt* configurations, symmetric with respect to the beam midpoint *Pt*. Bottom row represents L_1 and L_2 configurations. The circles have center (x_C,y_C) and radius $(1+\rho)/2$.

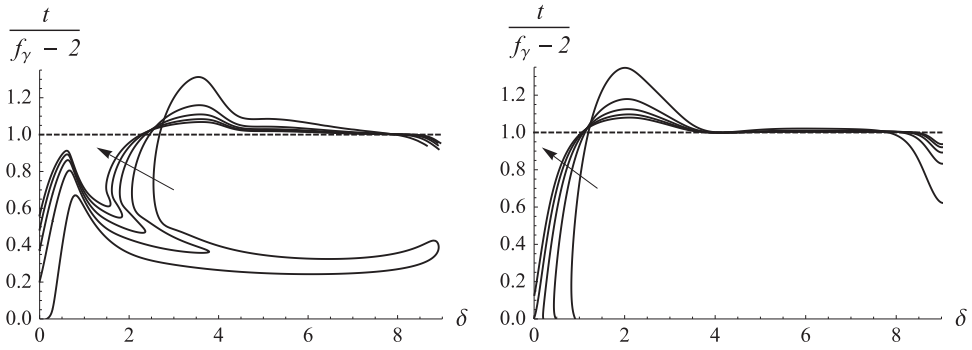

Fig. 7. Equilibrium paths for $f_\gamma=10,20,\ldots,50$ with the vertical axis rescaled according to Eq. (14). (Left) Axis-symmetric (*Ax*) configurations and (right) point-symmetric (*Pt*) configurations. Direction of increasing f_γ is indicated with the arrows.

We deposit a drop on a fibre with a known radius and we slowly bring the caliper forks closer to impose compression on the fibre. If the drop is able to coil the fibre, the macroscopic consequences are easily visible to the naked eye. If at first try the drop does not coil, the sample is tested again with a random compression and a slight shake to overcome any possible metastability. The couple drop/fiber is given an activity index of 1 if coiling is achieved and 0 otherwise (see Fig. 4). The experimental results show that coiling is present whenever $f_\gamma > \pi^2$, with a error of margin of 3%, consistent with Eq. (11).

5. Non-linear post-buckling computations

5.1. Equilibrium paths

We now analyze the post-buckling regime by numerically solving the non-linear system of equilibrium equations. We use a shooting method to solve the boundary-value problem (4)–(8) and a pseudo-arc-length continuation algorithm to follow the solution as parameters are varied, both these routines being implemented in Mathematica. For large f_γ values, typically $f_\gamma > 15$, numerical difficulties arise and we thankfully switch to the AUTO package [15]. We fix $\ell = 10$, $v_0 = 0.02$, $\rho = 0.2$, and we compute force-extension bifurcation diagrams for several values of f_γ. We show in Fig. 5 such a diagram for $f_\gamma = 20$ where the tension t is plotted as a function of the end-shortening $\delta = \ell - x(\ell)$. The diagram comprises four different equilibrium paths: (i) path *Ax* where configurations are symmetric with respect to the axis joining the center of the disk (x_C, y_C) and the beam midpoint $(x(\ell/2), y(\ell/2))$, (ii) path *Pt* where configurations are symmetric with respect to the beam midpoint, (iii) path L_1 where configurations are looping once inside the disk, and (iv) path L_2 where configurations are looping twice inside the disk. Few of these configurations are shown in Fig. 6. In a typical experiment the system is first completely straight, held by a large tension t. This situation corresponds to a point on the vertical axis of Fig. 5, above the buckling threshold. As t is decreased the systems reach the start of the *Ax* path, and the beam buckles. For $f_\gamma = 20$, the numerically found value of the buckling tension $t \simeq 3.66$ is to be compared to $t_b(20) \simeq 3.76$ given by (13), and $t \simeq 3.73$ given by (11). As the system branches on the *Ax* path, tension goes up again – we have a subcritical bifurcation. The slope of the *Ax* path is calculated analytically in Appendix B and is plotted in Fig. B1 for comparison. As the beam enters deeper in the post-buckling regime, bending localizes inside the disk and the tails remain approximatively straight. The path eventually reaches a plateau, see formula (14), where the beam coils in a circular way inside the disk and the bending energy in the beam can then be approximated by $(1/2)EI/R^2[L - X(L)]$. We also plot the $t > 0$ part of the path *Pt*. This path also reaches the same plateau as the beam coils in the same circular way inside the disk. In addition we plot paths along which the beam adopts configurations with one (path L_1) or two (path L_2) loops. The relevance of these paths could be questioned for two reasons: (i) configuration on path L_1 do not have the same topology as far as twist is considered: a full turn of twist would be necessary to connect configurations on path *Ax* or *Pt* with configurations on path L_1, see [16,17], and (ii) these paths are not connected to the vertical axis $\delta = 0$. We plot in Fig. 5 (right) the energy $\hat{E} = E_k + E_w + E_\gamma - P\gamma_{SV}L + F_\gamma(\Delta + D)$ as a function of the end-shortening δ and we see that, for some range of the end-shortening δ, configurations on paths L_1 or L_2have a lower energy than configurations on paths *Ax* or *Pt*. These remarks call for a stability analysis of the equilibrium configurations, as well as a study of configurations deformed in 3*D*, where twist, link, and writhe would be computed [18].

5.2. Approximate analytical model for the plateau regime

As explained in [6], in the regime where the end-shortening $\delta = \ell - x(\ell)$ is large, that is when several coils of the beam are present in the disk, the external tension t reaches a plateau and no longer varies as more coils are added. The plateau value of the tension is calculated by a balance of energy as a beam length ΔS enters the disk. The work done by the tension T is $-T\Delta S$, the work done by the meniscus force F_γ is $+F_\gamma \Delta S$, and the energy spent to bend the beam in coils is $-(1/2)(EI/R^2)\Delta S$. The sum of these energies is zero on the plateau, which yields

$$t = f_\gamma - 2 \tag{14}$$

in dimensionless quantities. In Fig. 7 we plot *Ax* and *Pt* equilibrium paths for $f_\gamma = 10, 20, \ldots, 50$ with the vertical axis rescaled according to (14). The collapse of the curves for $\delta \gtrsim 4$ confirms relation (14).

6. Conclusion

This paper presents a first venture into the complex equilibria adopted by a fiber buckled, coiled, and packed by a droplet. Using a simple 2D model and numerical continuation techniques, we have uncovered several equilibrium paths characterized by different symmetries (point-symmetric, axis-symmetric, single or double-looped) and provided clues for the bifurcations between these different states. Analytical predictions for the buckling threshold, as well as the asymptotic behavior (plateau regime) for the deep post-buckling regime have been derived. The agreement between experiments and theory for the windlass activation threshold is certainly promising, and calls for an extension of the present model to 3D (including twist and writhe), and a deeper comparison between the experimentally observed ordered and disordered packing modes and the theoretical prediction. Finally the deformation of the drop on its own, considered rigid throughout this study, and its interplay with the shape adopted by the fiber also deserves a dedicated investigation.

Acknowledgments

The present work was supported by ANR Grant ANR-09-JCJC-0022-01, ANR-14-CE07-0023-01, and ANR-13-JS09-0009. Financial support from 'La Ville de Paris – Programme Émergence' is also gratefully acknowledged, along with travel support from the Royal Society, through the International Exchanges Scheme (Grant IE130506) and support from the CNRS, through a PEPS-PTI Grant. We thank Christine Rollard (MNHN) for helpful discussions.

Appendix A. Variational derivation of the equilibrium equations

To prevent the beam from exiting the disk elsewhere than at the meniscus points, we use a (soft wall) barrier potential [14]

$$V(X,Y) = \frac{V_0}{1 + \rho - (1/R)\sqrt{(X - X_C)^2 + (Y - Y_C)^2}} \tag{A.1}$$

where the disk has center (X_C, Y_C) and radius R. The small dimensionless parameter ρ is introduced to avoid the potential to diverge at the meniscus points A and B, where the rod enters and exits the disk. The internal energy of the system comprises the bending energy E_b of the rod, the barrier energy E_w of the circle,

and surface energy E_γ

$$E_\kappa = \frac{1}{2}EI\int_0^{S_A}\kappa_1^2\,\mathrm{d}S + \frac{1}{2}EI\int_{S_A}^{S_B}\kappa_2^2\,\mathrm{d}S + \frac{1}{2}EI\int_{S_B}^{L}\kappa_3^2\,\mathrm{d}S \tag{A.2a}$$

$$E_w = \int_{S_A}^{S_B} V(X(S),Y(S),X_C,Y_C)\,\mathrm{d}S \tag{A.2b}$$

$$E_\gamma = P\gamma_{SV}S_A + P\gamma_{SL}(S_B-S_A) + P\gamma_{SV}(L-S_B) \tag{A.2c}$$

where $P=2\pi h$ is the perimeter of the cross-section of the rod, and V_0 has the dimension of an energy per unit length. The curvatures $\kappa_i(S)$ are defined in each region of the rod. We add the work done by the external load $T\boldsymbol{e_x}$ and obtain the potential energy of the system

$$E_\kappa + E_w + E_\gamma - TX(L) \tag{A.3}$$

We minimize this energy under the following constraints:

$$\frac{S_A+S_B}{2} = \frac{L}{2} \tag{A.4a}$$

$$[X(S_A)-X_C]^2 + [Y(S_A)-Y_C]^2 = R^2 \tag{A.4b}$$

$$[X(S_B)-X_C]^2 + [Y(S_B)-Y_C]^2 = R^2 \tag{A.4c}$$

Eq. (A.4a) imposes that the capturing disk is centered on the mid-point of the rod. We introduce Σ such that $S_A = L/2-\Sigma$ and $S_B = L/2+\Sigma$. The rod has then 2Σ of its arc-length spent in the disk. As the variables $X(S)$, $Y(S)$, $\kappa(S)$ and $\theta(S)$ all appear in the formulation, we have to consider the continuous constraints relating them:

$$X'(S) = \cos\theta(S), \quad Y'(S) = \sin\theta(S), \quad \theta'(S) = \kappa(S) \tag{A.5}$$

We consequently write the Lagrangian

$$\begin{aligned}
&\mathcal{L}(X,Y,\theta,\kappa_1,\kappa_2,\kappa_3,X_C,Y_C,\Sigma)\\
&\quad = -TX(L) + \int_0^{L/2-\Sigma}\left(\frac{EI}{2}\kappa_1^2 + P\gamma_{SV} + \nu_1(S)[X'-\cos\theta] + \mu_1(S)\right.\\
&\qquad \left.\times[Y'-\sin\theta] + \eta_1(S)[\theta'-\kappa_1]\right)\mathrm{d}S\\
&\qquad + \int_{L/2-\Sigma}^{L/2+\Sigma}\left(\frac{EI}{2}\kappa_2^2 + P\gamma_{SL} + \nu_2(S)[X'-\cos\theta]\right.\\
&\qquad +\mu_2(S)[Y'-\sin\theta] + \eta_2(S)[\theta'-\kappa_2] + \left.V(X,Y,X_C,Y_C)\right)\mathrm{d}S\\
&\qquad + \int_{L/2+\Sigma}^{L}\left(\frac{EI}{2}\kappa_3^2 + P\gamma_{SV} + \nu_3(S)[X'-\cos\theta]\right.\\
&\qquad +\mu_3(S)[Y'-\sin\theta] + \left.\eta_3(S)[\theta'-\kappa_3]\right)\mathrm{d}S\\
&\qquad + \frac{\Lambda_A}{2R}([X(L/2-\Sigma)-X_C]^2 + [Y(L/2-\Sigma)-Y_C]^2 - R^2)\\
&\qquad + \frac{\Lambda_B}{2R}([X(L/2+\Sigma)-X_C]^2 + [Y(L/2+\Sigma)-Y_C]^2 - R^2)
\end{aligned} \tag{A.6}$$

The rod is clamped as both extremities, boundary conditions read

$$X(0)=0, \quad Y(0)=0, \quad \theta(0)=0, \quad Y(L)=0, \quad \theta(L)=0 \tag{A.7}$$

A.1. First variation

We note $\boldsymbol{U} = (X,Y,\theta,\kappa_1,\kappa_2,\kappa_3,X_C,Y_C,\Sigma)$ and we consider the conditions for the state $\boldsymbol{U}_e$ to minimize the energy E. Calculus of variations shows that a necessary condition is

$$\mathcal{L}'(\boldsymbol{U}_e)\overline{\boldsymbol{U}} = \frac{\mathrm{d}}{\mathrm{d}\epsilon}\mathcal{L}(\boldsymbol{U}_e+\epsilon\overline{\boldsymbol{U}})\bigg|_{\epsilon=0} = 0 \tag{A.8}$$

where $\overline{\boldsymbol{U}} = (\overline{X},\overline{Y},\overline{\theta},\overline{\kappa}_1,\overline{\kappa}_2,\overline{\kappa}_3,\overline{X}_C,\overline{Y}_C,\overline{\Sigma})$. The bar ¯ sign represents a small perturbation of the variable. Moreover boundary conditions (A.7) imply that

$$\overline{X}(0)=0, \quad \overline{Y}(0)=0, \quad \overline{\theta}(0)=0, \quad \overline{Y}(L)=0, \quad \overline{\theta}(L)=0 \tag{A.9}$$

Noting that $\int_0^{A+\epsilon\overline{A}} f(x)\,dx = \int_0^A f(x)\,dx + \epsilon\overline{A}f(A) + O(\epsilon^2)$ we evaluate the first variation (A.8)

$$\begin{aligned}
&\mathcal{L}'(U_e)(\overline{U}) = -T\overline{X}(L) - 2F_\gamma\overline{\Sigma} + V_A\overline{\Sigma} + V_B\overline{\Sigma}\\
&\quad + \int_0^{L/2-\Sigma}(EI\overline{\kappa}_1\kappa_1 + \nu_1(S)[\overline{X}' + \overline{\theta}\sin\theta] + \mu_1(S)[\overline{Y}' - \overline{\theta}\cos\theta]\\
&\quad + \eta_1(S)[\overline{\theta}' - \overline{\kappa}_1])\,\mathrm{d}S\\
&\quad + \int_{L/2-\Sigma}^{L/2+\Sigma}(EI\overline{\kappa}_2\kappa_2 + \nu_2(S)[\overline{X}' + \overline{\theta}\sin\theta]\\
&\quad + \mu_2(S)[\overline{Y}' - \overline{\theta}\cos\theta] + \eta_2(S)[\overline{\theta}' - \overline{\kappa}_2] + \overline{V})\,\mathrm{d}S\\
&\quad \int_{L/2+\Sigma}^{L}(EI\overline{\kappa}_3\kappa_3 + \nu_3(S)[\overline{X}' + \overline{\theta}\sin\theta]\\
&\quad + \mu_3(S)[\overline{Y}' - \overline{\theta}\cos\theta] + \eta_3(S)[\overline{\theta}' - \overline{\kappa}_3])\,\mathrm{d}S\\
&\quad + \frac{\Lambda_A}{R}[X(L/2-\Sigma)-X_C][\overline{X}(L/2-\Sigma) - \overline{\Sigma}X'(L/2-\Sigma) - \overline{X}_C]\\
&\quad + \frac{\Lambda_A}{R}[Y(L/2-\Sigma)-Y_C][\overline{Y}(L/2-\Sigma) - \overline{\Sigma}Y'(L/2-\Sigma) - \overline{Y}_C]\\
&\quad + \frac{\Lambda_B}{R}[X(L/2+\Sigma)-X_C][\overline{X}(L/2+\Sigma) + \overline{\Sigma}X'(L/2+\Sigma) - \overline{X}_C]\\
&\quad + \frac{\Lambda_B}{R}[Y(L/2+\Sigma)-Y_C][\overline{Y}(L/2+\Sigma) + \overline{\Sigma}Y'(L/2+\Sigma) - \overline{Y}_C]
\end{aligned} \tag{A.10}$$

where $F_\gamma = P(\gamma_{SV}-\gamma_{SL})$, $V_A = V(X(S_A),Y(S_A))$, $V_B = V(X(S_B),Y(S_B))$, and $\overline{V} = (\partial V/\partial X)\overline{X} + (\partial V/\partial Y)\overline{Y} + (\partial V/\partial X_C)\overline{X}_C + (\partial V/\partial Y_C)\overline{Y}_C$. Note also that we have used (A.5) at $S = L/2 \pm \Sigma$ to eliminate several terms. Requiring (A.10) to vanish for all $\overline{\kappa}_i$, $i=1,2,3$, we obtain

$$EI\kappa_i(S) = \eta_i(S), \quad i=1,2,3 \tag{A.11}$$

and hence identify the Lagrange multipliers $\eta_i(S)$ with the bending moment $M(S)$ in the beam. Requiring (A.10) to vanish for all $\overline{\theta}$ yields, after integration by parts

$$\begin{aligned}
&[\eta_1(S)\overline{\theta}]_0^{L/2-\Sigma} + \int_0^{L/2-\Sigma}(\nu_1(S)\sin\theta - \mu_1(S)\cos\theta - \eta_1'(S))\overline{\theta}\,\mathrm{d}S\\
&\quad + [\eta_2(S)\overline{\theta}]_{L/2-\Sigma}^{L/2+\Sigma} + \int_{L/2-\Sigma}^{L/2+\Sigma}(\nu_2(S)\sin\theta - \mu_2(S)\cos\theta - \eta_2'(S))\overline{\theta}\,\mathrm{d}S\\
&\quad + [\eta_3(S)\overline{\theta}]_{L/2+\Sigma}^{L} + \int_{L/2+\Sigma}^{L}(\nu_3(S)\sin\theta - \mu_3(S)\cos\theta - \eta_3'(S))\overline{\theta}\,\mathrm{d}S = 0
\end{aligned} \tag{A.12}$$

Due to the boundary conditions (A.9), part of the boundary terms vanish. Nevertheless, arbitrariness of $\overline{\theta}$ at $S = L/2 \pm \Sigma$ implies that $\eta_1(L/2-\Sigma) = \eta_2(L/2-\Sigma)$ and $\eta_2(L/2+\Sigma) = \eta_3(L/2+\Sigma)$: the bending moment is continuous at the entry and the exit of the disk. Moreover, from the requirement that (A.1) vanishes for all $\overline{\theta}(S)$, we obtain the equations for the equilibrium of the bending moment

$$\eta_i'(S) = M'(S) = \nu_i(S)\sin\theta - \mu_i(S)\cos\theta, \quad i=1,2,3 \tag{A.13}$$

Requiring (A.10) to vanish for all $\overline{X}$ yields, after integration by parts

$$\begin{aligned}
&\frac{\Lambda_A}{R}[X(L/2-\Sigma)-X_C]\overline{X}(L/2-\Sigma) + [\nu_1(S)\overline{X}]_0^{L/2-\Sigma}\\
&\quad - \int_0^{L/2-\Sigma}\nu_1'(S)\overline{X}\,\mathrm{d}S - T\overline{X}(L)\\
&\quad + [\nu_2(S)\overline{X}]_{L/2-\Sigma}^{L/2+\Sigma} + \int_{L/2-\Sigma}^{L/2+\Sigma}\left[\frac{\partial V}{\partial X} - \nu_2'(S)\right]\overline{X}\,\mathrm{d}S\\
&\quad + \frac{\Lambda_B}{R}[X(L/2+\Sigma)-X_C]\overline{X}(L/2+\Sigma)\\
&\quad + [\nu_3(S)\overline{X}]_{L/2+\Sigma}^{L} - \int_{L/2+\Sigma}^{L}\nu_3'(S)\overline{X}\,\mathrm{d}S = 0
\end{aligned} \tag{A.14}$$

Boundary conditions (A.9) cancel part of the boundary terms, but arbitrariness of $\overline{X}$ at $S = L/2 \pm \Sigma$ implies

$$\nu_2(L/2-\Sigma) - \nu_1(L/2-\Sigma) = \frac{\Lambda_A}{R}[X(L/2-\Sigma)-X_C] \tag{A.15a}$$

$$\nu_3(L/2+\Sigma)-\nu_2(L/2+\Sigma)=\frac{\Lambda_B}{R}[X(L/2+\Sigma)-X_C] \tag{A.15b}$$

while arbitrariness of $\overline{X}$ at $S=L$ implies

$$\nu_3(L)=T \tag{A.16}$$

Eq. (A.16) enable us to identify ν_3 and therefore ν_1 and ν_2 with the x-component, N_x, of the resultant force in the beam. By extension the μ_i are identified to the y-component, N_y, of this force. Eqs. (A.15) are then seen as jumps in the x-component of the internal force due to the external force coming from the disk. Moreover, from the requirement that (A.14) vanishes for all $\overline{X}(S)$, we obtain the equilibrium equations for the x-component of the resultant force in the beam

$$\nu_1'(S)=0,\quad \nu_2'(S)=\frac{\partial V}{\partial X},\quad \nu_3'(S)=0 \tag{A.17}$$

The same procedure for the variable Y yields

$$\mu_2(L/2-\Sigma)-\mu_1(L/2-\Sigma)=\frac{\Lambda_A}{R}[Y(L/2-\Sigma)-Y_C] \tag{A.18a}$$

$$\mu_3(L/2+\Sigma)-\mu_2(L/2+\Sigma)=\frac{\Lambda_B}{R}[Y(L/2+\Sigma)-Y_C] \tag{A.18b}$$

and

$$\mu_1'(S)=0,\quad \mu_2'(S)=\frac{\partial V}{\partial Y},\quad \mu_3'(S)=0 \tag{A.19}$$

Eqs. (A.18) are then seen as jumps in the y-component of the internal force due to the external force coming from the disk, and Eqs. (A.19) are the equilibrium equations for the y-component of the resultant force in the beam. Requiring (A.10) to vanish for all $\overline{X}_C$ yields

$$-\frac{\Lambda_A}{R}[X(L/2-\Sigma)-X_C]-\frac{\Lambda_B}{R}[X(L/2+\Sigma)-X_C] + \int_{L/2-\Sigma}^{L/2+\Sigma}\frac{\partial V}{\partial X_C}\mathrm{d}S=0 \tag{A.20}$$

We use the identity $\frac{\partial V}{\partial X_C}=-\frac{\partial V}{\partial X}$ and (A.17) to obtain

$$\nu_2(L/2+\Sigma)-\nu_2(L/2-\Sigma)=-\frac{\Lambda_A}{R}[X(L/2-\Sigma)-X_C] -\frac{\Lambda_B}{R}[X(L/2+\Sigma)-X_C] \tag{A.21}$$

The same procedure for the variable Y_C yields

$$\mu_2(L/2+\Sigma)-\mu_2(L/2-\Sigma)=-\frac{\Lambda_A}{R}[Y(L/2-\Sigma)-Y_C] -\frac{\Lambda_B}{R}[Y(L/2+\Sigma)-Y_C] \tag{A.22}$$

Considering (A.21), (A.22), (A.15), and (A.18) together yields

$$\nu_1(L/2-\Sigma)=\nu_3(L/2+\Sigma) \tag{A.23}$$

$$\mu_1(L/2-\Sigma)=\mu_3(L/2+\Sigma) \tag{A.24}$$

which means that the internal force in the beam at the entrance of the disk is equal to the internal force at the exit of the disk. We therefore have that the total external force applied on the beam by the disk is zero. Finally requiring that (A.10) vanishes for all $\overline{\Sigma}$ yields

$$\begin{aligned}&-2F_\gamma+V_A+V_B-\frac{\Lambda_A}{R}\{[X(L/2-\Sigma)-X_C]X'(L/2-\Sigma)\\&\quad+[Y(L/2-\Sigma)-Y_C]Y'(L/2-\Sigma)\}\\&\quad+\frac{\Lambda_B}{R}\{[X(L/2+\Sigma)-X_C]X'(L/2+\Sigma)\\&\quad+[Y(L/2+\Sigma)-Y_C]Y'(L/2+\Sigma)\}=0\end{aligned} \tag{A.25}$$

In summary the equilibrium of the beam is governed by the system

$$X'(S)=\cos\theta \tag{A.26a}$$

$$Y'(S)=\sin\theta \tag{A.26b}$$

$$EI\theta'(S)=M \tag{A.26c}$$

$$M'(S)=N_x\sin\theta-N_y\cos\theta \tag{A.26d}$$

$$N_x'(S)=\chi\frac{\partial V}{\partial X}+\delta(S-S_A)\Lambda_A\frac{X_A-X_C}{R}+\delta(S-S_B)\Lambda_B\frac{X_B-X_C}{R} \tag{A.26e}$$

$$N_y'(S)=\chi\frac{\partial V}{\partial Y}+\delta(S-S_A)\Lambda_A\frac{Y_A-Y_C}{R}+\delta(S-S_B)\Lambda_B\frac{Y_B-Y_C}{R} \tag{A.26f}$$

with $\chi=1$ for $S\in[S_A;S_B]$ and $\chi=0$ otherwise, and where $\delta(S-S_\star)$ is the Dirac distribution centered on $S=S_\star$ and $X_{A,B}=X(\frac{L}{2}\pm\Sigma)$ and $Y_{A,B}=Y(\frac{L}{2}\pm\Sigma)$.

Appendix B. Incipient post-buckling regime

We here focus on configurations on path Ax. With regard to the shifted arc-length variable $\hat{s}=s-\ell/2$, introduced in Section 3, the variables have the following symmetries:

$$x(-\hat{s})=2x_C-x(\hat{s}),\quad y(-\hat{s})=y(\hat{s}),\quad \theta(-\hat{s})=-\theta(\hat{s}) \tag{B.1a}$$

$$m(-\hat{s})=m(\hat{s}),\quad n_x(-\hat{s})=n_x(\hat{s}),\quad n_y(-\hat{s})=-n_y(\hat{s}) \tag{B.1b}$$

The variable $n_y(\hat{s})$, an odd function of $\hat{s}$, has also to verify (A.24), which reads $n_y(\hat{s}=-\sigma)=n_y(\hat{s}=\sigma)$. Consequently $n_y(\pm\sigma)=0$ and, as $n_y(\hat{s})$ is constant for $|\hat{s}|>\sigma$, we have that $n_y(\hat{s})\equiv 0,\ \forall|\hat{s}|>\sigma$. Moreover, in the limit where the barrier potential tends to zero, $v_0\to 0$,[1] $n_y'(\hat{s})\equiv 0$ inside the disk. Being an odd function, $n_y(\hat{s})$ is then such that

$$n_y(\hat{s})\equiv 0\quad\forall\hat{s} \tag{B.2}$$

The consequence is that the force jumps (A.18) for $n_y(\hat{s})$ at the entry $\hat{s}=-\sigma$ and exit $\hat{s}=+\sigma$ of the disk are zero: $\lambda_A[y_A-y_C]=0=\lambda_B[y_B-y_C]$. We discard the cases $\lambda_A=0$ and $\lambda_B=0$ for which there would not be any meniscus force at all, and conclude

$$y_A=y_C=y_B \tag{B.3}$$

Conditions (A.4b) and (A.4c) now read $(x_A-x_C)^2=1/4$ and $(x_B-x_C)^2=1/4$ which yields

$$x_A=x_C-1/2\quad\text{and}\quad x_B=x_C+1/2 \tag{B.4}$$

As $n_x(-\hat{s})=n_x(\hat{s})$, the force jumps (A.15) imply that $\lambda_A[x_A-x_C]+\lambda_B[x_B-x_C]=0$. Using (B.4), we conclude that

$$\lambda_A=\lambda_B \tag{B.5}$$

Finally, using the global force balance (A.25), (B.3), (B.4), and (B.5), and still in the limit $v_0\to 0$, we obtain

$$f_\gamma=\lambda_B\cos\theta_B \tag{B.6}$$

Taking advantage of the symmetries (B.1), we now rewrite the boundary-value problem (4)–(6) for the interval $\hat{s}\in[0,\ell/2]$. Using the external tension t, we write the x-component of the force as $n_x(\hat{s})\equiv t,\ \forall\hat{s}\in[\sigma,\ell/2]$ and using the jumps at $\hat{s}=\sigma$ we obtain $n_x(\hat{s})\equiv t-\lambda<0,\ \forall\hat{s}\in(0,\sigma)$ where we note $\lambda=\lambda_A=\lambda_B$. We therefore have to solve

$$\begin{aligned}&\mathrm{d}x^{\mathrm{in}}/\mathrm{d}\hat{s}=\cos\theta^{\mathrm{in}},\quad \mathrm{d}\theta^{\mathrm{in}}/\mathrm{d}\hat{s}=m^{\mathrm{in}},\\&\quad \mathrm{d}m^{\mathrm{in}}/\mathrm{d}\hat{s}=-(\lambda-t)\sin\theta^{\mathrm{in}}\quad\text{for }\hat{s}\in[0,\sigma]\end{aligned} \tag{B.7a}$$

$$\mathrm{d}x^{\mathrm{out}}/\mathrm{d}\hat{s}=\cos\theta^{\mathrm{out}},\quad \mathrm{d}\theta^{\mathrm{out}}/\mathrm{d}\hat{s}=m^{\mathrm{out}},$$

[1] The repulsion from the disk is only important for configurations in the deep post-buckling regime.

$$\mathrm{d}m^{\mathrm{out}}/\mathrm{d}\hat{s} = -(\lambda - t)\sin\theta^{\mathrm{out}} \quad \text{for } \hat{s} \in [\sigma, \ell/2] \tag{B.7b}$$

These are six differential equations with two unknowns parameters λ and σ. Boundary conditions are

$$x^{\mathrm{in}}(0) = x_C, \quad \theta^{\mathrm{in}}(0) = 0, \quad x^{\mathrm{in}}(\sigma) = x_C + 1/2,$$
$$f_\gamma = \lambda\cos\theta^{\mathrm{in}}(\sigma), \quad \theta^{\mathrm{out}}(\ell/2) = 0 \tag{B.8}$$

and matching conditions are

$$x^{\mathrm{out}}(\sigma) = x^{\mathrm{in}}(\sigma), \quad \theta^{\mathrm{out}}(\sigma) = \theta^{\mathrm{in}}(\sigma), \quad m^{\mathrm{out}}(\sigma) = m^{\mathrm{in}}(\sigma) \tag{B.9}$$

Hence, for each given value of t, f_γ, ℓ, the eight boundary and matching conditions define a well-posed problem for Eqs. (B.7). For simplicity reasons, we replace the last condition in (B.8) by $\theta^{\mathrm{out}}(+\infty) = 0$, that is we work in the large ℓ limit. We look for a small amplitude solution to this boundary-value problem, that is we develop each variable in power of ϵ, where ϵ is a small parameter. As buckling happens through a pitchfork bifurcation, two symmetric ($\epsilon > 0$, where the beam is buckled upward, and $\epsilon < 0$, where the beam is buckled downward) branches emerge from the $\epsilon = 0$ buckling point. Taking advantage of this symmetry we introduce the following series:

$$x^{\mathrm{in,out}}(\hat{s}) = x_C + \hat{s} + \epsilon^2 x_2^{\mathrm{in,out}}(\hat{s}) + O(\epsilon^4) \tag{B.10}$$

$$\theta^{\mathrm{in,out}}(\hat{s}) = \epsilon\theta_1^{\mathrm{in,out}}(\hat{s}) + \epsilon^3\theta_3^{\mathrm{in,out}}(\hat{s}) + O(\epsilon^5) \tag{B.11}$$

$$m^{\mathrm{in,out}}(\hat{s}) = \epsilon m_1^{\mathrm{in,out}}(\hat{s}) + \epsilon^3 m_3^{\mathrm{in,out}}(\hat{s}) + O(\epsilon^5) \tag{B.12}$$

$$t = t_0 + \epsilon^2 t_2 + O(\epsilon^4) \tag{B.13}$$

$$\lambda = f_\gamma + \epsilon^2\lambda_2 + O(\epsilon^4) \tag{B.14}$$

$$\sigma = 1/2 + \epsilon^2\sigma_2 + O(\epsilon^4) \tag{B.15}$$

Solving the problem (B.7)–(B.9), we find at order ϵ^1 that

$$\theta_1^{\mathrm{in}}(\hat{s}) = \sin(\hat{s}\sqrt{f - t_0}) \tag{B.16}$$

$$\theta_1^{\mathrm{out}}(\hat{s}) = e^{\sqrt{t_0}/2}\sin\left(\frac{\sqrt{f - t_0}}{2}\right)e^{-\hat{s}\sqrt{t_0}} \tag{B.17}$$

and that t_0 is solution to the equation

$$\sqrt{f - t_0}\cos\left(\frac{\sqrt{f - t_0}}{2}\right) + \sqrt{t_0}\sin\left(\frac{\sqrt{f - t_0}}{2}\right) = 0 \tag{B.18}$$

which is (12). At order ϵ^2, we find

$$\lambda_2 = \frac{1}{2}f_\gamma\sin^2\left(\frac{\sqrt{f - t_0}}{2}\right) \tag{B.19}$$

$$\sigma_2 = \frac{\sqrt{f - t_0} - \sin\left(\sqrt{f - t_0}\right)}{8\sqrt{f - t_0}} \tag{B.20}$$

$$x_2^{\mathrm{in}}(\hat{s}) = \frac{\sin(2\hat{s}\sqrt{f - t_0}) - 2\hat{s}\sqrt{f - t_0}}{8\sqrt{f - t_0}} \tag{B.21}$$

$$x_2^{\mathrm{out}}(\hat{s}) = \frac{\sin(\sqrt{f - t_0})}{8\sqrt{f - t_0}} - \frac{1}{8} + \frac{\sin^2\left(\frac{\sqrt{f - t_0}}{2}\right)(e^{(1-2\hat{s})\sqrt{t_0}} - 1)}{4\sqrt{t_0}} \tag{B.22}$$

At order ϵ^3, we find $\theta_3^{\mathrm{in}}(\hat{s})$, $m_3^{\mathrm{in}}(\hat{s})$, $\theta^{\mathrm{out}}(\hat{s})$, and $m^{\mathrm{out}}(\hat{s})$ and from their matching conditions (B.9), we obtain

$$t_2 = \frac{f_\gamma^2(4 + 5\sqrt{t_0}) - f_\gamma t_0(2 + 3\sqrt{t_0}) + 2t_0^2 - 2f_\gamma[f_\gamma(\sqrt{t_0} - 2) + 4t_0]\cos(\sqrt{f - t_0})}{8f_\gamma(2 + \sqrt{t_0})} \tag{B.23}$$

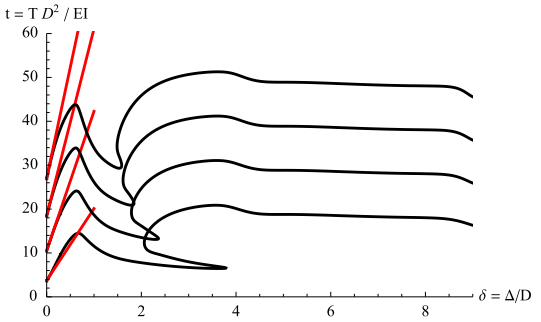

Fig. B1. Paths Ax for $f_\gamma = 20, 30, 40$ and 50 with their slope at the origin given by (B.25).

We now compute the end-shortening $\delta = \ell - x(s = \ell) = \ell - 2[x^{\mathrm{out}}(\hat{s} = \ell/2) - x_C]$, still in the limit where $\ell \to +\infty$. Using (B.10) and (B.22) we find $\delta = \epsilon^2\delta_2$ with

$$\delta_2 = \frac{1}{4} + \frac{\sin^2\left(\frac{\sqrt{f - t_0}}{2}\right)}{2\sqrt{t_0}} - \frac{\sin\sqrt{f - t_0}}{4\sqrt{f - t_0}} \tag{B.24}$$

Finally we write

$$t = t_0 + \epsilon^2 t_2 = t_0 + \frac{t_2}{\delta_2}\delta \tag{B.25}$$

We plot in Fig. B1 paths Ax for $f_\gamma = 20, 30, 40$ and 50 and the straight lines given by (B.25).

References

[1] R. Foelix, Biology of Spiders, Oxford University Press, Oxford, 2010.
[2] F.G. Omenetto, D.L. Kaplan, New opportunities for an ancient material, Science 329 (5991) (2010) 528–531.
[3] F. Vollrath, D.P. Knight, Liquid crystalline spinning of spider silk, Nature 410 (6828) (2001) 541–548.
[4] N. Becker, E. Oroudjev, S. Mutz, J.P. Cleveland, P.K. Hansma, C.Y. Hayashi, D.E. Makarov, H.G. Hansma, Molecular nanosprings in spider capture-silk threads, Nat. Mater. 2 (4) (2003) 278–283.
[5] F. Vollrath, D.T. Edmonds, Modulation of the mechanical properties of spider silk by coating with water, Nature 340 (6231) (1989) 305–307.
[6] H. Elettro, S. Neukirch, F. Vollrath, A. Antkowiak, In-drop Capillary Spooling of Spider Capture Thread Inspires Highly Extensible Fibres, arXiv:1501.00962, 2015.
[7] N. Stoop, J. Najafi, F.K. Wittel, M. Habibi, H.J. Herrmann, Packing of elastic wires in spherical cavities, Phys. Rev. Lett. 106 (2011) 214102.
[8] R. Vetter, F.K. Wittel, H.J. Herrmann, Morphogenesis of filaments growing in flexible confinements, Nat. Commun. 5 (2014).
[9] L. Boué, M. Adda-Bedia, A. Boudaoud, D. Cassani, Y. Couder, A. Eddi, M. Trejo, Spiral patterns in the packing of flexible structures, Phys. Rev. Lett. 97 (16) (2006) 166104.
[10] E. Couturier, S. Courrech du Pont, S. Douady, The filling law: a general framework for leaf folding and its consequences on leaf shape diversity, J. Theoret. Biol. 289 (2011) 47–64.
[11] J.C. LaMarque, T.-v.L. Le, S.C. Harvey, Packaging double-helical DNA into viral capsids, Biopolymers 73 (3) (2004) 348–355.
[12] W.S. Klug, M.T. Feldmann, M. Ortiz, Three-dimensional director-field predictions of viral DNA packing arrangements, Comput. Mech. 35 (2) (2005) 146–152.
[13] A. Leforestier, F. Livolant, Structure of toroidal DNA collapsed inside the phage capsid, Proc. Natl. Acad. Sci. 106 (23) (2009) 9157–9162.
[14] R.S. Manning, G.B. Bulman, Stability of an elastic rod buckling into a soft wall, Proc. R. Soc. A: Math. Phys. Eng. Sci.: Math. 461 (2060) (2005) 2423–2450.
[15] E. Doedel, H.B. Keller, J.P. Kernevez, Numerical analysis and control of bifurcation problems: bifurcation in infinite dimensions, Int. J. Bifurc. Chaos 01 (04) (1991) 745–772.
[16] G.H.M. van der Heijden, S. Neukirch, V.G.A. Goss, J.M.T. Thompson, Instability and self-contact phenomena in the writhing of clamped rods, Int. J. Mech. Sci. 45 (1) (2003) 161–196.
[17] V.G.A. Goss, G.H.M. van der Heijden, J.M.T. Thompson, S. Neukirch, Experiments on snap buckling, hysteresis and loop formation in twisted rods, Exp. Mech. 45 (2) (2005) 101–111.
[18] H. Elettro, S. Neukirch, A. Antkowiak, Equilibrium and stability of a twisted rod confined in a liquid drop, 2015, in preparation.